PASJ: Publ. Astron. Soc. Japan **60**, S11–S24, 2008 February 20

Reproducibility of Non–X-Ray Background for the X-Ray Imaging Spectrometer aboard Suzaku

Noriaki TAWA, Kiyoshi HAYASHIDA, Masaaki NAGAI, Hajime NAKAMOTO, and Hiroshi TSUNEMI
Department of Earth and Space Science, Graduate School of Science, Osaka University, Toyonaka, Osaka 560-0043
tawa@ess.sci.osaka-u.ac.jp
Hiroya YAMAGUCHI
Department of Physics, Graduate School of Science, Kyoto University, Sakyo-ku, Kyoto 606-8502
Yoshitaka ISHISAKI
Department of Physics, Tokyo Metropolitan University, 1-1 Minami-Osawa, Hachioji, Tokyo 192-0397
Eric D. MILLER
Kavli Institute for Astrophysics and Space Research, Massachusetts Institute of Technology, Cambridge, MA 02139, USA
Tsunefumi MIZUNO
Department of Physical Science, Hiroshima University, 1-3-1 Kagamiyama, Higashi-Hiroshima, Hiroshima 739-8526
Tadayasu DOTANI and Masanobu OZAKI
Institute of Space and Astronautical Science, Japan Aerospace Exploration Agency, 3-1-1 Yoshino-dai, Sagamihara, Kanagawa 229-8510
and
Haruyoshi KATAYAMA
Japan Aerospace Exploration Agency (JAXA), 2-1-1 Sengen, Tsukuba, Ibaraki 305-8505

(Received 2007 June 24; accepted 2007 October 26)

Abstract

One of the advantages of the X-ray Imaging Spectrometer (XIS) system aboard Suzaku is its low and stable non–X-ray background (NXB). In order to make the best use of this advantage, modeling the NXB spectra with high accuracy is important to subtract them from the spectra of on-source observations. We are constructing an NXB database by collecting XIS events when the the dark Earth covers the XIS FOV. The total exposure time of the NXB data is presently about 785 ks for each XIS. It is found that the count rate of the NXB anti-correlates with the cut-off-rigidity and correlates with the count rate of the PIN upper discriminator (PIN-UD) in the Hard X-ray Detector aboard Suzaku. We thus model the NXB spectrum for a given on-source observation by employing either of these parameters, and obtain a better reproducibility of the NXB for the model with PIN-UD than that with the cut-off-rigidity. The reproducibility of the NXB model with PIN-UD is 4.55–5.63% for each XIS NXB in the 1–7 keV band and 2.79–4.36% for each XIS NXB in the 5–12 keV band for each 5 ks exposure of the NXB data. This NXB reproducibility is much smaller than the spatial fluctuation of the cosmic X-ray background in the 1–7 keV band, and is almost comparable to that in the 5–12 keV band.

Key words: instrumentation: detectors — methods: data analysis — X-rays: general

1. Introduction

The X-ray Imaging Spectrometer (XIS) at the foci of the four X-ray telescopes (XRT) aboard the Suzaku observatory are the best suited among the recent X-ray astronomy satellites, such as ASCA (Burke et al. 1991), Chandra (Weisskopf et al. 2002), and XMM (Lumb et al. 2000), for diffuse and low surface brightness sources owing to their large collection area and low and stable background level. One of the XIS, XIS 1, has a back-illuminated (BI) CCD, while the other three XISs, XISs 0, 2, 3, are equipped with front-illuminated (FI) CCDs (hereafter referred to as XIS-FIs; Koyama et al. 2007). The background levels normalized by the effective area and the field of view (FOV), in terms of the S/N ratio to diffuse emissions, of the XIS-FIs are comparable to those of the ASCA SIS (Mitsuda et al. 2007). Moreover, these background levels are ~ 3 and ~ 10-times lower than those of the XMM EPIC and the Chandra ACIS at 5 keV, respectively (Mitsuda et al. 2007).

The background of the XIS consists of three components: (1) non–X-ray background (NXB); (2) a solar component, which is emission from Earth's atmosphere, illuminated by the Sun and solar wind charge exchange; and (3) a diffuse X-ray component from such sources as a local hot bubble (LHB), galactic diffuse X-ray emissions, and cosmic X-ray background (CXB).

While the X-ray background is produced by emission within the XRT FOV, the XIS NXB is caused by charged particles and γ-rays (Mizuno et al. 2004) entering the detector from various directions. Therefore, the NXB varies with time according to the radiation environment of the satellite, i.e. the particle or γ-ray spectra hitting Suzaku. Since the altitude of the orbit of Suzaku is lower than that of XMM or Chandra, the particle and γ-ray spectra of Suzaku are different from that of XMM or Chandra. Although these spectra are not entirely clear, the intensities of those from Suzaku are relatively lower and more stable than those of XMM or Chandra. In the case of XMM EPIC, solar soft protons produce flares of up to 10-times the quiescent background level, and affect 30–40% of the XMM

observation time (Carter & Read 2007). However, this component hardly affects Suzaku.

The solar component (2) includes the fluorescence lines of nitrogen and oxygen from the atmosphere of Earth and scattered solar X-rays. The intensity of the solar component depends on both the solar activity and the elevation angle from the sunlit Earth edge. This component can be minimized by filtering data based on the elevation angle from the sunlit Earth edge. Emission lines of nitrogen and oxygen are enhanced through charge exchange between interplanetary and geocoronal neutral atoms and metal ions in the solar-wind (Fujimoto et al. 2007). Referring to the solar wind data, proton or X-ray fluxes, helps to evaluate of this component.

The spectrum of the CXB is approximated by a power-law spectrum having a photon index of ~ 1.4 in the 2–10 keV band (Kushino et al. 2002). The CXB is known to be a collection of faint unresolved extragalactic sources (Hasinger et al. 2001). It is uniform over the sky with some fluctuation. The LHB and galactic diffuse X-ray emissions are dominant below 1 keV, and their spectra depend on the direction of the sky. Snowden et al. (1997) proposed a model that provides their spectra based on the ROSAT all-sky survey.

Among the three components of the XIS background, the solar component is time variable and the most difficult to model. We try to minimize it by using the orbital and altitude data, which are elevation angles from the day or night Earth edge, and the solar-wind data. The diffuse X-ray component is basically stable, and can be evaluated by observing other fields by Suzaku. The target of this paper is to properly estimate the NXB, so that we can use it as a background model. It is most important to establish a method to accurately evaluate the NXB spectra and time variations in order to maximize the advantage of the low background level of the XIS. We have thus constructed an XIS NXB database to be used in evaluating the NXB and have introduced a method to generate the NXB model, given the intensity of charged particles. We have also examined and confirmed the reproducibility of our NXB model.

2. NXB of the XIS

2.1. NXB Database

We constructed a database of the XIS NXB from events collected while Suzaku was pointed toward the night Earth (NTE). Under this condition, the diffuse X-ray component (3) was blocked, and the solar component (2) did not contaminate. The criteria with which we selected the NTE events were as follows:

- Rev0.7 products (Mitsuda et al. 2007), of which the XIS mode was the normal 5×5 or 3×3 mode (without burst or window options). The events were further filtered with the condition of T_SAA_HXD > 436 s, where T_SAA_HXD means the time after passage of the South Atlantic Anomaly (SAA). This criterion was used in revision 1.2 or 1.3 products (Mitsuda et al. 2007), and this filtering excluded flares in the NXB intensity just after Suzaku passed through the SAA. The events during the telemetry saturation were also excluded.
- Cleansis in FTOOLS was applied with the default parameters to exclude any flickering pixels.
- The NTE events were extracted for Earth elevation angles (ELV) less than $-5°$, and Earth day-time elevation angles (DYE_ELV) greater than $100°$.

Since the XIS was in its initial operation during 2005 August, we collected the NTE events from data observed between 2005 September and 2006 May with the above criteria. The total exposure time of the NTE data was ~ 785 ks for each XIS. The NXB database[1] consists of the NTE event files and the associated enhanced house keeping (EHK) file, in which orbital information is listed with time. Two associated tools, *mk_corsorted_spec_v1.0.pl* and *mk_corweighted_bgd_v1.1.pl*, to generate the NXB model using the cut-off-rigidity, were also prepared. Since the event files in the database can be processed with various FTOOLS including XSELECT, the NXB spectra can be easily created. The subject of this paper is to generate the most appropriate NXB spectra for a given observation.

We hereafter refer to "NTE events" as the NXB events, and, refer to the data comprising the NXB events as the "NXB data". Additionally, the "NXB database" indicates a data set that contains the NXB event files and the associated EHK file.

2.2. NXB Spectra

Figure 1 shows the NXB spectra of XIS 0 and XIS 1. The spectra were extracted from the whole region of the CCD, except for the calibration source regions (two corners of the CCD chip, Koyama et al. 2007). The XIS FOV is ~ 287 arcmin^2, which is 91% of the FOV of the whole CCD chip. The spectra show fluorescence lines of Al, Si, Au, Mn, and Ni in the XIS and XRT. Table 1 gives the intensities of these emission lines, and table 2 gives the origin for each fluorescence line. The XIS 0 has relatively strong Mn-K emission

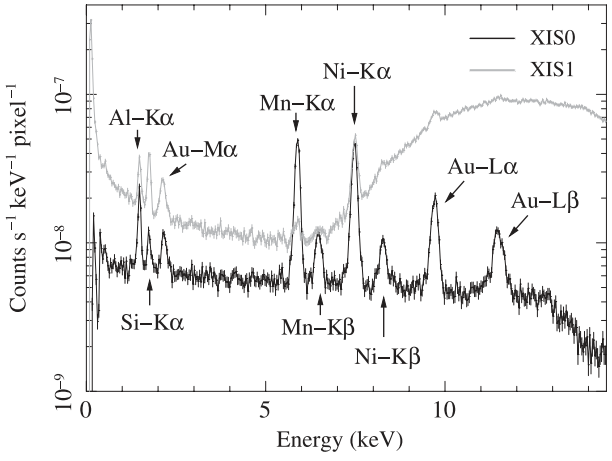

Fig. 1. Spectra of the NXB in the XIS 0 (black) and the XIS 1 (gray).

[1] The first version of the database is accessible via Suzaku web page at ISAS/JAXA ⟨ http://www.astro.isas.jaxa.jp/suzaku/analysis/xis/nte/ ⟩ and GSFC/NASA ⟨ http://heasarc.gsfc.nasa.gov/docs/suzaku/analysis/xisbgd0.html ⟩, but the NXB data in this database lack T_SAA_HXD and telemetry saturation filtering described here, leading to a total exposure of 800 ks. The second version (the product of this paper) will be released in 2007 October.

Table 1. Energies and count rates of the line components in the NXB spectra.

Line	Energy	Count rate* (10^{-9} counts s^{-1} pixel^{-1})			
	(keV)	XIS 0	XIS 1	XIS 2	XIS 3
Al-Kα	1.486	1.45 $\pm$0.11	1.84 $\pm$ 0.14	1.41 $\pm$0.10	1.41 $\pm$0.10
Si-Kα	1.740	0.479 $\pm$ 0.081	2.27 $\pm$ 0.15	0.476 $\pm$ 0.080	0.497 $\pm$ 0.082
Au-Mα	2.123	0.63 $\pm$0.093	1.10 $\pm$ 0.13	0.776 $\pm$ 0.097	0.619 $\pm$ 0.092
Mn-Kα	5.895	6.92 $\pm$0.19	0.43 $\pm$ 0.14	1.19 $\pm$0.13	0.76 $\pm$0.11
Mn-Kβ	6.490	1.10 $\pm$0.11	0.26 $\pm$ 0.13	0.40 $\pm$0.11	0.253 $\pm$ 0.094
Ni-Kα	7.470	7.12 $\pm$0.19	7.06 $\pm$ 0.37	8.01 $\pm$0.20	7.50 $\pm$0.20
Ni-Kβ	8.265	0.96 $\pm$0.10	0.75 $\pm$ 0.22	1.16 $\pm$0.11	1.18 $\pm$0.11
Au-Lα	9.671	3.42 $\pm$0.15	4.15 $\pm$ 0.49	3.45 $\pm$0.15	3.30 $\pm$0.15
Au-Lβ	11.51	2.04 $\pm$0.14	1.93 $\pm$ 0.48	1.97 $\pm$0.14	1.83 $\pm$0.14

* The count rates are obtained from the whole CCD chip excluding the calibration source regions. Errors are at 90% confidence level.

Table 2. Origins of the fluorescent lines in the NXB spectra.

Lines	Origins
Al-Kα	Optical blocking filter, housing, alumina substrate to mount CCD
Si-Kα	CCD (Si fluorescent line)
Au-Mα, Lα, Lβ	Housing, CCD substrate, heatsink
Mn-Kα, Kβ	Scattered X-rays from calibration sources
Ni-Kα, Kβ	Housing, heatsink

lines at 5.9 and 6.5 keV, as shown in table 1. This is due to stray X-rays from the ^{55}Fe calibration source, although why the radiation was detected outside of the calibration source regions remains unknown (Yamaguchi et al. 2006). Since the XIS-FIs have a thick neutral layer beneath the depletion layer, most of the background events generated by charged particles produce charge over many pixels, and are rejected as ASCA grade-7 events.[2] On the other hand, the XIS 1 (BI-CCD) has a relatively thin depletion layer, and almost no neutral layer, resulting in relatively many background events in grades 0, 2, 3, 4, and 6 (Yamaguchi et al. 2006). Therefore, the background count rate of the XIS 1 is higher than those of the XIS-FIs, especially above $\sim$ 7 keV, as shown in figure 1.

2.3. *Cut-off-Rigidity and PIN-UD*

Since the NXB is caused by charged particles, the NXB should depend on the intensity of charged particles striking Suzaku, which is strongly correlated with the geomagnetic cut-off-rigidity. We introduce a new type of cut-off-rigidity, *COR2*, for Suzaku. The calculation for *COR2* is independent from that for the conventional cut-off-rigidity, *COR*. *COR* has been employed in the analysis of Tenma, Ginga, ASCA, and Suzaku. We summarize the characteristics of *COR* and *COR2* in appendix 1. In the main text, we use *COR2* when discussing the NXB.

Suzaku carries a non-imaging hard X-ray instrument, the Hard X-ray Detector (HXD). The HXD sensor contains 4×4 well-type phoswich units (well units) with 4 PIN silicon diodes in each (Takahashi et al. 2007; Kokubun et al. 2007). When a charged particle generates a large signal in a PIN silicon diode, the PIN upper discriminator (PIN-UD) is activated at a threshold of around 90 keV. This can be a good monitor of the real-time intensity of the charged particles striking Suzaku. The number of PIN-UD counts is recorded with each well unit. We sum up the PIN-UD count rates for all well units and average them for each 32 seconds to reduce the statistical error. The typical number of PIN-UD counts in 32 seconds is $\sim$5100, by summing up all well units. We hereafter call this count rate the PIN-UD. Figure 2 shows the PIN-UD as a function of *COR2*. There is a strong anti-correlation between PIN-UD and *COR2*. However, the anti-correlation is widely distributed. This is because PIN-UD mirrors the real-time intensity of the charged particles, while *COR2* is calculated from a *COR* map (shown in figure 12b) and the orbital position of Suzaku. Therefore, *COR2* might not correctly reproduce the real-time intensity of the charged particles. In addition, some events deviate from the correlation, as shown in regions A and B of figure 2. The events in regions A occurred just before Suzaku entered the SAA. The events in region B occurred at the time when Suzaku passed near the region of (longitude, latitude) = (350°, 19°). We assume that this is because the *COR2* values in this region were approximately calculated, as shown in appendix 1. However, the number of events in regions A and B is less than 1% of the total number. We will discuss which parameters of *COR2* or PIN-UD can correctly reproduce NXB in the next section.

[2] The ASCA grade shows the spread of an event. In the case of the XIS, we consider that most of the X-ray events do not split into a region larger than 2×2 pixels. Grade-7 events, in which the spread of event contains more than 2×2 pixels, are regarded as background events (Koyama et al. 2007).

Figure 3a shows the count rate of NXB for each XIS in the 5–12 keV energy band as a function of *COR2*. The count rate of each bin of XIS 1 is about 6-times higher than those of XIS-FIs. This is because XIS 1 has a relatively thin depletion layer and almost no neutral layer, as discussed in subsection 2.2. Therefore, the NXB intensity of XIS 1 depends on the intensity of charged particles as well as the XIS-FIs. On the other hand, the spectra are different between the low *COR2* region (*COR2* $\leq$ 8 GV) and the high *COR2* region (*COR2* $>$ 8 GV), as shown in figure 3b. The differences mainly appear in the normalization of the spectra. The periods of the NXB variations primarily correspond to the orbital period of Suzaku, 96 minutes, since NXB depends on the cut-off-rigidity. We should also note that NXB did not have any apparent long-term changes during 9 months. For details, we will discuss this matter in subsections 3.3 and section 4.

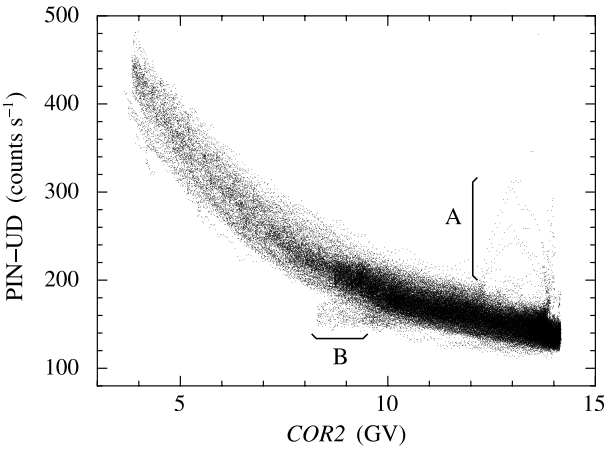

Fig. 2. PIN-UD as a function of *COR2*. PIN-UD is anti-correlated with *COR2*, although there is a noticeable scatter, such as the regions A and B. The events in region A occurred just before Suzaku entered the SAA. The events in region B occurred at the time when Suzaku passed near the region of (longitude, latitude) = (350°, 19°).

Since the *COR2* and the NXB count rates are anti-correlated, we can use *COR2* to estimate the NXB spectra to be subtracted as background for a given observation. PIN-UD can also be used as such a parameter to estimate the NXB spectra, considering the anti-correlation between *COR2* and PIN-UD. In the following section, we attempt to model the NXB spectra from the NXB data by employing either of *COR2* or PIN-UD. The two kinds of NXB models, one with *COR2* and the other with PIN-UD, are compared based on their reproducibilities.

3. NXB Models and Their Reproducibility

3.1. *NXB Models: NXB Data Sorted by COR2 or PIN-UD*

In order to correctly subtract NXB from an on-source observation, we introduce a method to model NXB. Since the spectra of charged particles and γ-rays causing NXB are not fully understood, this is a semi-empirical method. We prepared two tools, *mk_corsorted_spec* and *mk_corweighted_bgd*,[3] to generate the NXB model. Mk_corsorted_spec is used to sort with a modeling parameter, i.e. *COR2* or PIN-UD, bin and generate the NXB spectra for each modeling parameter bin. Mk_corweighted_bgd is used to generate the NXB model spectrum for a given on-source observation by summing up the sorted spectra with appropriate weights. The weighted NXB model spectrum, $S_{\rm w}$, is expressed as follows:

$$S_{\rm w} = \frac{\sum_{i=1}^{n} T_i S_i}{\sum_{i=1}^{n} T_i} = \sum_{i=1}^{n} \frac{T_i}{T_{\rm total}} S_i \ , \qquad (1)$$

where the modeling parameter is sorted into n bins. T_i and S_i are the exposure time of the on-source observation and the spectrum of the NXB data in the ith modeling parameter bin, respectively. $T_{\rm total}$ is the total exposure time of the on-source observation. Equation (1) makes equal the modeling parameter distribution for the on-source observation and that for the NXB data.

We sorted the NXB and on-source data into 14 bins with either *COR2* or PIN-UD. The *COR2* and PIN-UD bins are

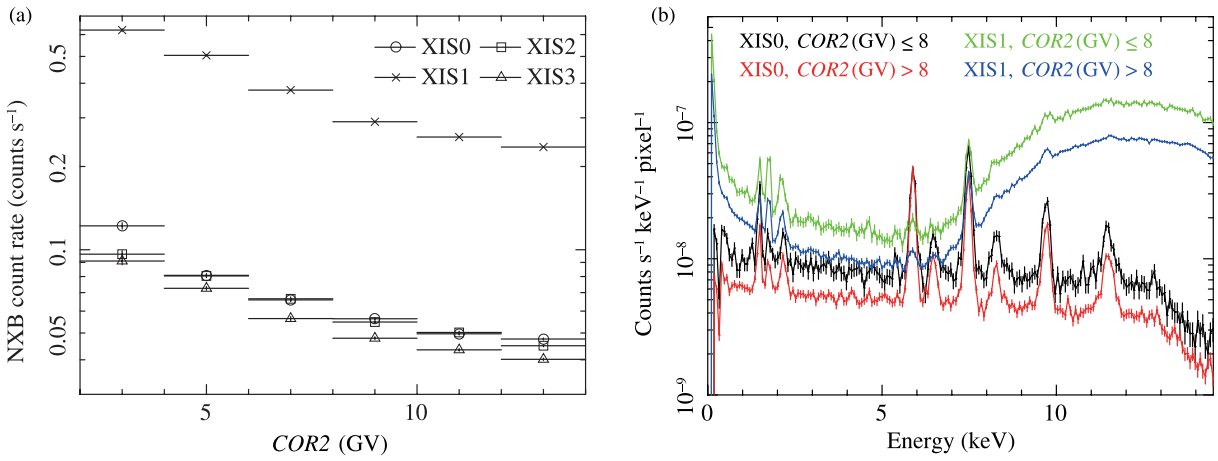

Fig. 3. (a) *COR2* dependence of NXB (average count rate in 5–12 keV) for each XIS. (b) NXB spectra in *COR2* $\leq$ 8 and *COR2* $>$ 8 GV. Black and red lines show the XIS 0 spectra. Green and blue lines show the XIS 1 spectra. The NXB count rate is anti-correlated with *COR2*, and the count rate of XIS 1 is higher than those of XIS-FIs.

Table 3. The PIN-UD and the *COR2* bins ranges.

Bin #	PIN-UD	Count rate*	Exposure†	*COR2*	Count rate*	Exposure†
	(counts s^{-1})	10^{-2} (counts s^{-1})	(ks)	(GV)	10^{-2} (counts s^{-1})	(ks)
1	100–150	4.551 ± 0.051	175.4	15 –12.8	4.746 ± 0.048	208.3
2	150–175	4.857 ± 0.045	236.6	12.8–10.5	4.877 ± 0.045	246.2
3	175–200	5.329 ± 0.062	137.7	10.5–9.1	5.347 ± 0.061	142.6
4	200–225	5.533 ± 0.089	70.0	9.1–8.1	5.73 ± 0.10	53.6
5	225–250	6.24 ± 0.15	28.3	8.1–7.3	6.24 ± 0.15	27.6
6	250–275	6.74 ± 0.18	20.7	7.3–6.6	6.49 ± 0.18	19.2
7	275–300	6.85 ± 0.20	17.9	6.6–6.0	7.17 ± 0.20	17.5
8	300–325	7.83 ± 0.23	14.3	6.0–5.5	7.29 ± 0.24	13.0
9	325–350	7.42 ± 0.23	13.6	5.5–5.1	7.83 ± 0.27	10.8
10	350–375	8.35 ± 0.26	12.5	5.1–4.7	7.52 ± 0.25	12.2
11	375–400	9.33 ± 0.27	12.4	4.7–4.3	8.60 ± 0.28	11.3
12	400–425	10.61 ± 0.31	10.8	4.3–4.0	9.55 ± 0.32	9.5
13	425–450	11.53 ± 0.48	4.9	4.0–3.7	11.37 ± 0.39	7.3
14	450–500	7.4 ± 1.3	0.4	3.7–2.0	13.74 ± 0.59	4.0

* The count rates are obtained from the NXB data of the XIS 0 in the 5–12 keV band. Errors are at 1σ confidence level.
† The exposure times are obtained from the NXB data of the XIS 0.

defined as shown in table 3. In addition, table 3 gives the NXB count rate (5–12 keV) and exposure time for each *COR2* and PIN-UD bin in the XIS 0. We defined the bin ranges at even intervals of the PIN-UD, and set the *COR2* bins so as to obtain approximately comparable count rates of the corresponding PIN-UD bins. We should note that the NXB model obtained by sorting into even intervals with the exposure time has a comparable level to that by sorting into the bins given in table 3.

3.2. Reproducibility of the NXB Models

We first calculate the intrinsic variability of the NXB data to compare with the reproducibility of the NXB model. The standard deviation of the NXB count rate contains a systematic error and a statistical error. We define the systematic error (1σ confidence level) as the intrinsic variability. To calculate the intrinsic variability, we divide the NXB data into 5 ks exposure bins (generally spanning a few days) and obtain the count rate for each. Since the NXB intensity is particularly low, the count rates are obtained in the 5–12 keV energy band to reduce the statistical error. There are typically 250 counts per 5 ks exposure bin in this energy range for XIS-FIs. Figure 4 shows the distribution of this count rate, hereafter called C_j for the jth bin. We calculate the standard deviation of C_j ($\sigma_{\rm c}$) as follows:

$$\sigma_{\rm c}^2 = \frac{1}{n-1}\sum_{j=1}^{n}(C_j - \mu_{\rm c})^2 \,, \tag{2}$$

where n is the number of the 5 ks NXB data, and $\mu_{\rm c}$ is the average of C_i, $\mu_{\rm c} = (1/N)\sum_{j=1}^{n} C_j$. Then, the statistical error of C_j is assumed by Poisson statistics, and is calculated by $\sqrt{C_j/T_j}$, where T_j is the exposure time of the jth bin (in this case, T_j is 5 ks). Since we divided the NXB data into 5 ks exposure, the statistical error of each C_j is approximately constant. We therefore obtain the statistical error contained in $\sigma_{\rm c}$ ($\sigma_{\rm sta,c}$) as follows:

$$\sigma_{\rm sta,c} = \frac{1}{n}\sum_{j=1}^{n}\sqrt{\frac{C_j}{T_j}} \,. \tag{3}$$

We then calculate the systematic error ($\sigma_{\rm sys,c}$) as follows:

$$\sigma_{\rm sys,c} = \sqrt{\sigma_{\rm c}^2 - \sigma_{\rm sta,c}^2} \,. \tag{4}$$

$\sigma_{\rm sys,c}$ is the intrinsic variability, and is summarized in table 4. The intrinsic variability shows the reproducibility of the NXB without being modeled. Details about the errors of $\sigma_{\rm c}$, $\sigma_{\rm sta,c}$, and $\sigma_{\rm sys,c}$ given in table 4, are presented in appendix 2.

We next calculate the reproducibility of the NXB model described in equation (1). The NXB spectra, S_i in equation (1), are obtained from the NXB data according to the modeling parameter. The weights of each bin, $T_i/T_{\rm total}$ in equation (1), are calculated by the modeling parameter for each 5 ks NXB data bin. We thus obtain the NXB models for each 5 ks bin and calculated the residual, data minus model. The jth residual (ΔC_j) is calculated by $C_j - M_j$, where M_j is the count rate of the NXB model for the jth 5 ks NXB data bin. There are two kinds of ΔC_j, ΔC_{COR2} and $\Delta C_{\rm PIN\text{-}UD}$, which are calculated based on *COR2* and PIN-UD, respectively. Figure 5 shows the distributions of ΔC_{COR2} and $\Delta C_{\rm PIN\text{-}UD}$ in the 5–12 keV energy band. These distributions are relatively narrow compared with the distribution of C_j shown in figure 4. This indicates that the NXB models correctly reproduce the NXB data. Since the way to calculate the reproducibility is the same with ΔC_{COR2} and $\Delta C_{\rm PIN\text{-}UD}$, we express this by ΔC_j. The standard deviation of ΔC_j ($\sigma_{\Delta \rm c}$) is calculated as follows:

[3] These tools are new versions of mk_corsorted_spec_v1.0.pl and mk_corweighted_bgd_v1.1.pl. These support the *COR* only. We will merge the new tools in one and release it as xisnxbgen in FTOOLS.

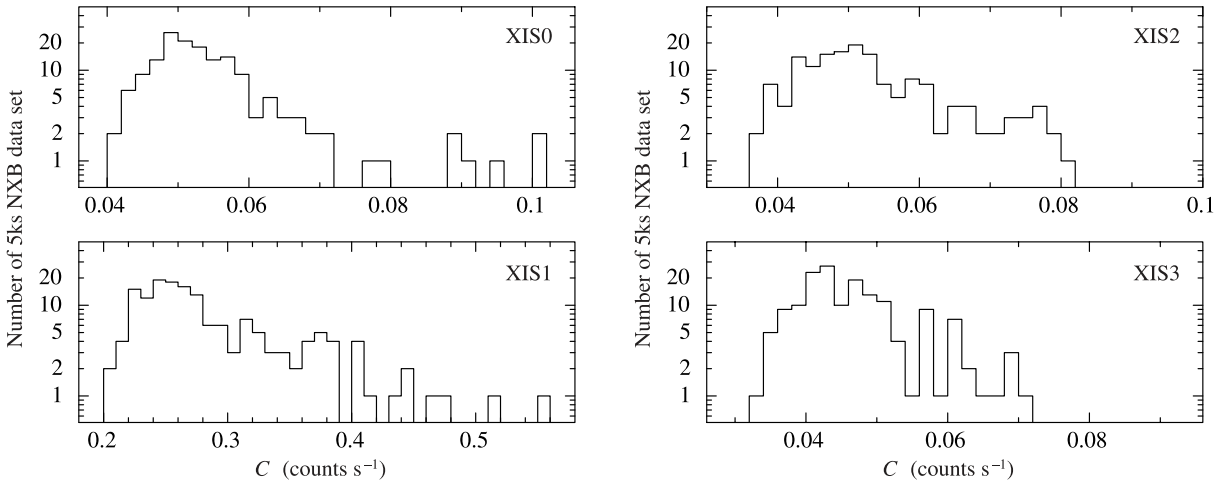

Fig. 4. Distribution of C_j in the XIS 0, 1, 2, and 3. C_j is calculated in the 5–12 keV energy band.

Table 4. Statistical summary of the NXB data.

Sensor	Average count rate* (10^{-2} counts s^{-1})	Standard deviation† (%)	Statistical error† (%)	Intrinsic variability† (%)
XIS 0	5.464 ± 0.026	19.2 ± 1.1	6.03 ± 0.34	18.2 ± 1.1
XIS 1	28.758 ± 0.060	22.5 ± 1.3	2.62 ± 0.15	22.4 ± 1.3
XIS 2	5.317 ± 0.026	19.1 ± 1.1	6.11 ± 0.35	18.1 ± 1.1
XIS 3	4.685 ± 0.024	16.85 ± 0.95	6.51 ± 0.37	15.5 ± 1.0

* The count rates are obtained from the NXB data in the 5–12 keV band. Errors are at 1σ confidence level.
† These values are normalized by the average count rate.

$$\sigma^2_{\Delta c} = \frac{1}{n-1}\sum_{j=1}^{n}(\Delta C_j - \mu_{\Delta c})^2 , \quad (5)$$

where $\mu_{\Delta c}$ is the average of ΔC_j and is expected to be zero. The statistical error of ΔC_j is $\sqrt{C_j/T_j + M_j/T}$, where T is total exposure time of the NXB data. The average of these statistical errors ($\sigma_{\mathrm{sta},\Delta c}$) is expressed as follows:

$$\sigma_{\mathrm{sta},\Delta c} = \frac{1}{n}\sum_{j=1}^{n}\sqrt{\frac{C_j}{T_j} + \frac{M_j}{T}} . \quad (6)$$

Since $T \sim 157 T_j$, the value of $\sigma_{\mathrm{sta},\Delta c}$ is approximately $\sigma_{\mathrm{sta,c}}$ [equation (3)]. By using $\sigma_{\Delta c}$ and $\sigma_{\mathrm{sta},\Delta c}$, the systematic error of ΔC_j ($\sigma_{\mathrm{sys},\Delta c}$) is calculated as

$$\sigma_{\mathrm{sys},\Delta c} = \sqrt{\sigma^2_{\Delta c} - \sigma^2_{\mathrm{sta},\Delta c}} . \quad (7)$$

Hear, $\sigma_{\mathrm{sys},\Delta c}$ is defined as the "reproducibility" of the NXB model. We independently calculated the reproducibility for each XIS, and show them in table 5a. Details about the errors of the reproducibilities are presented in appendix 2. Since the PIN-UD sometimes exceeds the range of 100–500 counts s^{-1}, the total exposure time reduces to ~ 760 ks. On the other hand, for the NXB model with *COR2*, the whole NXB data set of ~ 785 ks is available. The reproducibilities of the NXB models (table 5a) are about 1/3 of the intrinsic variability of the NXB count rate (table 4). However, the residuals sometimes become large in both NXB models, as shown in figure 5.

Table 5. Reproducibilities of two kinds of the NXB models.*

NXB	Sensor	*COR2*† (%)	PIN-UD† (%)
(a) Unfiltered	XIS 0	6.60 ± 0.61	8.12 ± 0.68
	XIS 1	7.18 ± 0.46	5.57 ± 0.39
	XIS 2	10.33 ± 0.77	7.85 ± 0.68
	XIS 3	3.32 ± 0.56	3.42 ± 0.57
(b) *NXB1*	XIS 0	4.05 ± 0.55	2.67 ± 0.53
	XIS 1	6.32 ± 0.43	4.81 ± 0.36
	XIS 2	9.77 ± 0.76	8.49 ± 0.72
	XIS 3	4.09 ± 0.59	4.11 ± 0.60
(c) *NXB2*	XIS 0	3.54 ± 0.61	2.79 ± 0.60
	XIS 1	6.95 ± 0.53	4.36 ± 0.39
	XIS 2	5.67 ± 0.69	3.96 ± 0.64
	XIS 3	2.34 ± 0.64	3.82 ± 0.68

* Calculated for the 5 ks NXB data in the 5–12 keV energy band.
† These values are normalized by the average count rate shown in table 4. Errors are at 1σ confidence level.

3.3. *Improvements to the NXB Model by Filtering the Data*

To further improve the reproducibilities of the NXB models, we examined the time and orbital position of Suzaku when the count rate significantly deviated from the NXB model, i.e., > 0.01 counts s^{-1} for the XIS-FIs in figure 5. We found that those data were obtained from 2005/10/09 ($t = 1.822 \times 10^8$ s,

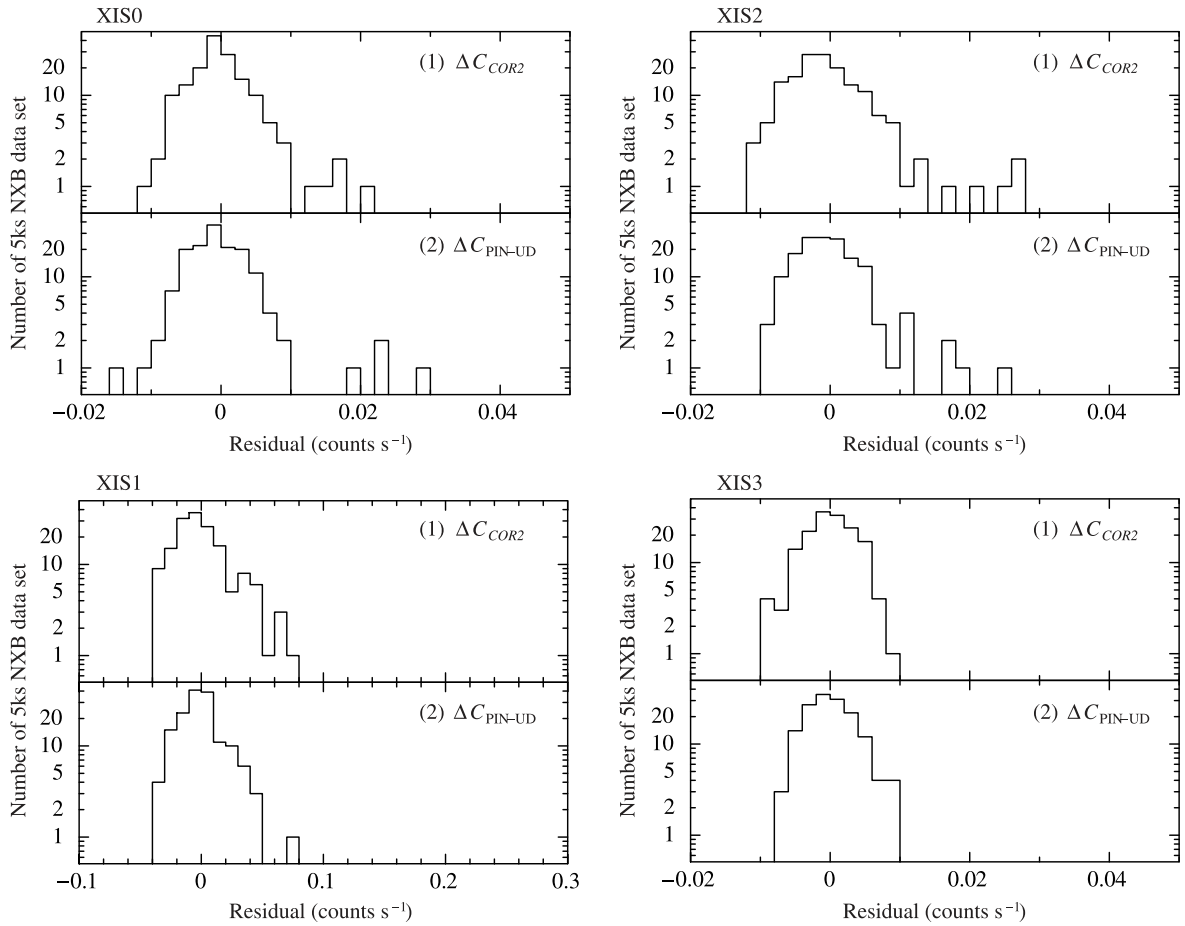

Fig. 5. Distributions of (1) ΔC_{COR2}, and (2) $\Delta C_{\rm PIN\text{-}UD}$ in the XIS 0, 1, 2, and 3.

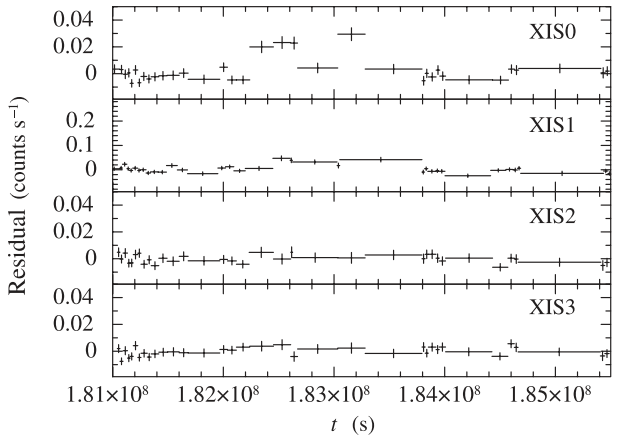

Fig. 6. Light curve of $\Delta C_{\rm PIN\text{-}UD}$ in the XIS 0, 1, 2, and 3. The residuals were obtained from unfiltered NXB data in the 5–12 keV band.

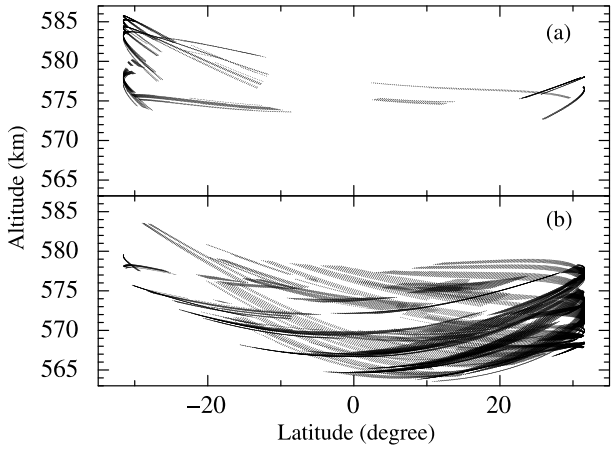

Fig. 7. Orbital positions of Suzaku for XIS observations of the NTE during (a) period A and (b) other times.

where t is time since 2000/01/01 00:00:00) to 2005/10/28 ($t = 1.838 \times 10^8$ s) and from 2005/11/29 ($t = 1.866 \times 10^8$ s) to 2005/12/20 ($t = 1.884 \times 10^8$ s). We call these time periods period A. Figure 6 shows the light curve of $\Delta C_{\rm PIN\text{-}UD}$. The count rate of $\Delta C_{\rm PIN\text{-}UD}$ increases during the first time period of period A, especially in XIS 0.

Figure 7a shows the orbital position during period A, and figure 7b shows the orbital position at other times. These plots indicate that the residuals increase when Suzaku passes through high latitude and high altitude regions. We therefore exclude any NXB events during the time when the orbital positions of Suzaku are latitude $\leq -23°$, altitude ≥ 576.5 km or latitude $\geq 29°$, altitude ≥ 577.5 km (hereafter the "orbit filter")

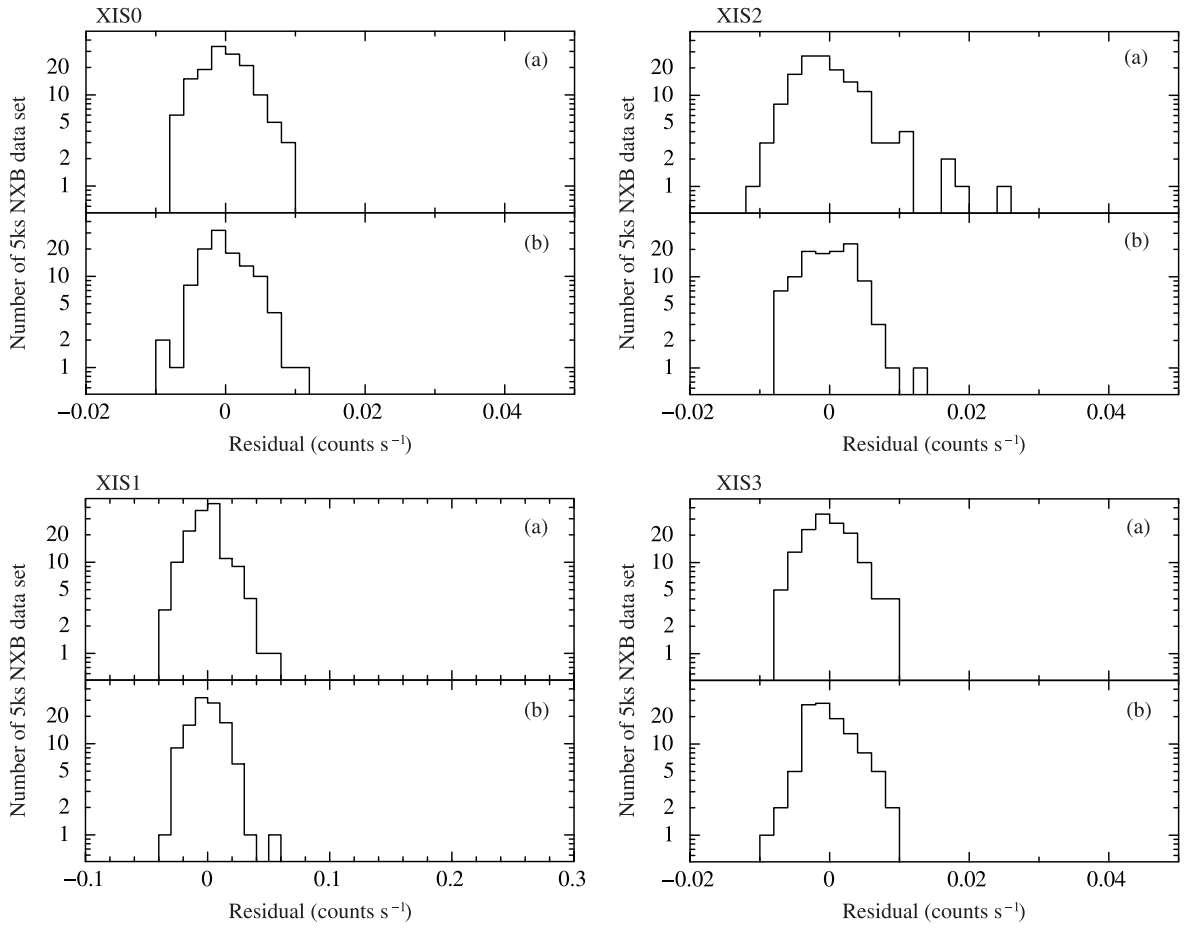

Fig. 8. Distribution of $\Delta C_{\rm PIN\text{-}UD}$ in the XIS 0, 1, 2, and 3. The residuals were obtained from (a) the *NXB1* and (b) the *NXB2* data in 5–12 keV energy band.

from the NXB data. The total exposure time of the NXB data with the orbit filter (hereafter "*NXB1*") is $\sim$730 ks, while that with the PIN-UD is $\sim$710 ks. The reproducibilities of the NXB models for the *NXB1* data are independently evaluated for each XIS by the same way as that described in subsection 3.2. Figure 8a shows the distribution of $\Delta C_{\rm PIN\text{-}UD}$ obtained from the *NXB1* data, and table 5b gives their reproducibilities. We can improve the reproducibilities by employing an orbit filter. Especially, the reproducibility of the XIS 0 is 3-times better than that without this filter.

The NXB model of XIS 2 with the orbit filter applied has almost the same level of reproducibility as that without the orbit filter. In addition, the reproducibility of XIS 2 is the worst among the XIS-FIs (XIS 0, 2, 3) (tables 5a and 5b). We therefore consider the long-term variation of the NXB intensity. Figure 9 shows a light curve of $\Delta C_{\rm PIN\text{-}UD}$ obtained from the *NXB1* data. We found that $\Delta C_{\rm PIN\text{-}UD}$ during 2005 September had been higher than that after 2005 October, especially in XIS 2. We speculate that this is because the solar activity was particularly high during 2005 September. The proton and solar X-ray intensities are continuously monitored by the Geostationary Operational Environmental Satellites (GOES).[4]

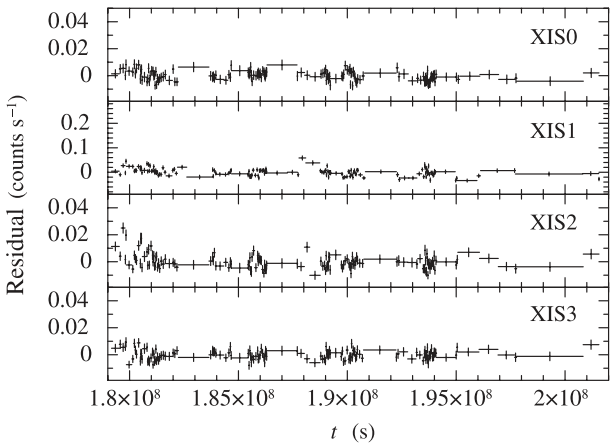

Fig. 9. Light curve of $\Delta C_{\rm PIN\text{-}UD}$ in the XIS 0, 1, 2, and 3. The residuals were obtained from the *NXB1* data in 5–12 keV energy band.

These intensities in 2005 September frequently exceeded 100 times those of the normal state of the Sun. We fitted the light curve after 2005 October with a linear function, finding that the NXB intensities of the XIS-FIs were constant with time within $\pm$6% per year. On the other hand, the NXB intensity of XIS 1 decreased with a gradient of (-7.8 ± 5.8)% per year

[4] The GOES data are available at ⟨http://www.ngdc.noaa.gov/stp/GOES/goes.html⟩.

Table 6. Reproducibilities of the NXB models.

Sensor	Average count rate 10^{-2} (counts s^{-1})	Statistical error* (%)	Reproducibility*† *COR2* (%)	PIN-UD (%)
XIS 0	4.163 ± 0.027	6.94 ± 0.47	5.06 ± 0.74	4.55 ± 0.74
XIS 1	7.321 ± 0.036	5.22 ± 0.35	7.55 ± 0.71	5.63 ± 0.63
XIS 2	3.871 ± 0.026	7.19 ± 0.49	7.31 ± 0.84	5.18 ± 0.78
XIS 3	3.475 ± 0.025	7.59 ± 0.52	6.34 ± 0.84	4.76 ± 0.80

* These values are normalized by the average count rate. Errors are at 1σ confidence level.
† Reproducibilities of the NXB models which are calculated by dividing the *NXB2* data into 5 ks exposure bins in the 1–7 keV energy band.

Table 7. Reproducibilities of the NXB models.*

Energy range (keV)	Sensor	Statistical error† (%)	Reproducibility† *COR2* (%)	PIN-UD (%)
1–7	XIS 0	2.29 ± 0.54	1.89 ± 0.84	2.02 ± 0.90
	XIS 1	1.72 ± 0.39	2.61 ± 0.80	2.70 ± 0.81
	XIS 2	2.37 ± 0.56	1.73 ± 0.84	0.31 ± 0.79
	XIS 3	2.50 ± 0.59	2.08 ± 0.92	1.20 ± 0.88
5–12	XIS 0	1.96 ± 0.46	1.03 ± 0.66	1.89 ± 0.79
	XIS 1	0.85 ± 0.19	2.98 ± 0.72	2.36 ± 0.59
	XIS 2	1.98 ± 0.47	1.87 ± 0.75	1.20 ± 0.72
	XIS 3	2.14 ± 0.50	1.51 ± 0.75	0.40 ± 0.72

* Calculated by dividing the *NXB2* data into 50 ks exposure bins.
† These values are normalized by the average count rate in the energy bands of the 1–7 keV (table 6) or the 5–12 keV (table 4). Errors are at 1σ confidence level.

(90% confidence level). However, since the gradient is small, we continue to apply the same method of modeling as the XIS-FIs to XIS 1.

We therefore exclude the NXB events during 2005 September from the *NXB1* data (hereafter "*NXB2*") and independently evaluate their reproducibilities for each XIS. Figure 8b shows the distribution of $\Delta C_{\mathrm{PIN\text{-}UD}}$ obtained from the *NXB2* data, and table 5c shows their reproducibilities. Better reproducibilities than the unfiltered NXB data can be obtained for all of the XIS. In addition, we found that the NXB model with the PIN-UD has better reproducibility than that with *COR2*. The total exposure time of this *NXB2* data is ~ 560 ks, but for the PIN-UD model, the exposure time is ~ 550 ks. Since the exposure time is long enough, excluding the data during 2005 September is not a serious problem for the observations after 2005 October.

3.4. Reproducibility of the NXB for the 1–7 keV Band

We evaluated the reproducibility of the NXB in the 1–7 keV energy band by the same method as that described in subsection 3.2. The CXB is dominant compared with the NXB in this energy band. Table 6 gives the average count rate, statistical error, and reproducibility for the 5 ks *NXB2* data. The reproducibilities are as good as those for the 5–12 keV energy band (table 5c), and the NXB model with the PIN-UD has better reproducibility than that with *COR2*.

3.5. Reproducibility with Longer Exposure Data

We have so far calculated the NXB reproducibility by dividing the NXB data into each 5 ks exposure bins. Here, we examine the NXB reproducibility for a longer exposure time of 50 ks, typical for on-source observations. Each 50 ks NXB exposure typically spans a few weeks. Table 7 gives the reproducibilities of the NXB models for an exposure time of 50 ks in the energy bands of 1–7 keV and 5–12 keV. The reproducibilities of the 50 ks NXB models are improved from those for the 5 ks NXB models. This is because any fluctuations of the residuals were smoothed by integrating for a long time.

4. Subtraction of the NXB from on-Source Observation

In this section, we consider the practical manner of how to subtract the NXB for on-source science observations. First, since the intensity of the NXB is not uniform over the CCD chip (Yamaguchi et al. 2006), the NXB spectrum needs to be extracted from the same region as the source spectrum in the detector (DET) coordinates (Ishisaki et al. 2007). We can extract the NXB spectra sorted by the cut-off-rigidity for a given region defined in the DET coordinates with the mk_corsorted_spec (same applies to the mk_corsorted_spec_v1.0.pl). Next, the sorted NXB spectra are summed up with appropriate weights calculated for the on-source observation using the mk_corweighted_bgd (same

applies to the mk_corweighted_bgd_v1.1.pl). The summed-up spectrum is the NXB model to be subtracted from on-source spectra.

One of the problems in this procedure is the presence of emission-line components in the NXB spectra. These components are time-dependent; the energy resolution of the XIS degrades with time (Koyama et al. 2007), and the intensities of the Mn-K emission lines decrease with the half life of ^{55}Fe, 2.73 years. Since the NXB data contained in the NXB database were made from the NXB events between 2005 September and 2006 May, and this time dependence was not taken into account, the emission-line components in the NXB spectra could not be reproduced correctly for a given on-source observation. This problem became prominent for observations after 2006 June. Figure 10 shows an example of a raw on-source spectrum and the NXB model spectrum, which we have described above. These are the averaged spectra of the XIS-FIs.

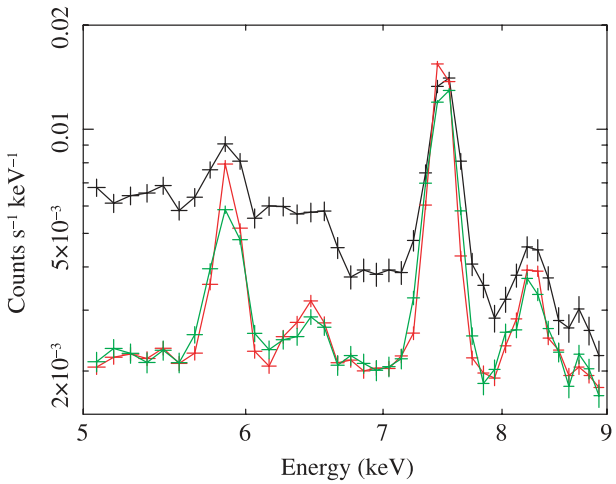

Fig. 10. (black) On-source observation spectrum. (red) The NXB model spectrum without the correction for the emission line components. (green) The NXB model spectrum with the correction for the emission-line components. These are averaged spectra of XIS-FIs.

Figure 11a shows the on-source spectrum from which the NXB model spectrum was subtracted, black minus red line shown in figure 10. This on-source spectrum was obtained in the observation of the link region between the galaxy clusters A 399 and A 401 taken during 2006 August 19–22 with an exposure time of 150 ks (observation ID is 801020010. For details, see Fujita et al. 2007). The model in figure 11a is a single thermal model (APEC in XSPEC) plus a power-law model. The thermal model represents the intracluster medium, and the power-law model represents the CXB. These are the same models as those used by Fujita et al. (2007). Significant residuals are visible at energies of Mn-Kα (5.9 keV) and Ni-Kα (7.4 keV) in figure 11a. We therefore developed a way to deal with these emission-line components in the NXB spectra, as follows:

1. The NXB model spectrum was constructed with *COR2* or PIN-UD using the method described in subsection 3.1.
2. The line components (Mn-Kα, Mn-Kβ, Ni-Kα, Ni-Kβ, and Au-Lα) in the NXB model spectrum were fitted with the redistribution matrix file (RMF) for 2005 August observations, at which point the degradation of the energy resolution was negligible. For example, in the energy range of 5.5–7.0 keV, where there are Mn-Kα and Mn-Kβ lines, the spectrum was fitted with two Gaussians plus a power-law continuum. We set the line widths of the two Gaussian components as free parameters. The emission lines of Ni-Kα, Ni-Kβ, and Au-Lα were similarly fitted.
3. We simulated the spectrum of the five Gaussian components using the *fakeit* command in XSPEC, using the fitting parameters determined in step 2.
4. The spectrum created in the step 3 was subtracted from the NXB model spectrum from step 1. This should correspond to the NXB continuum spectrum from which the five Gaussian line components were removed.
5. We added the simulated line components to the NXB continuum spectrum created in step 4, using the fakeit command. To take into account the degradation of

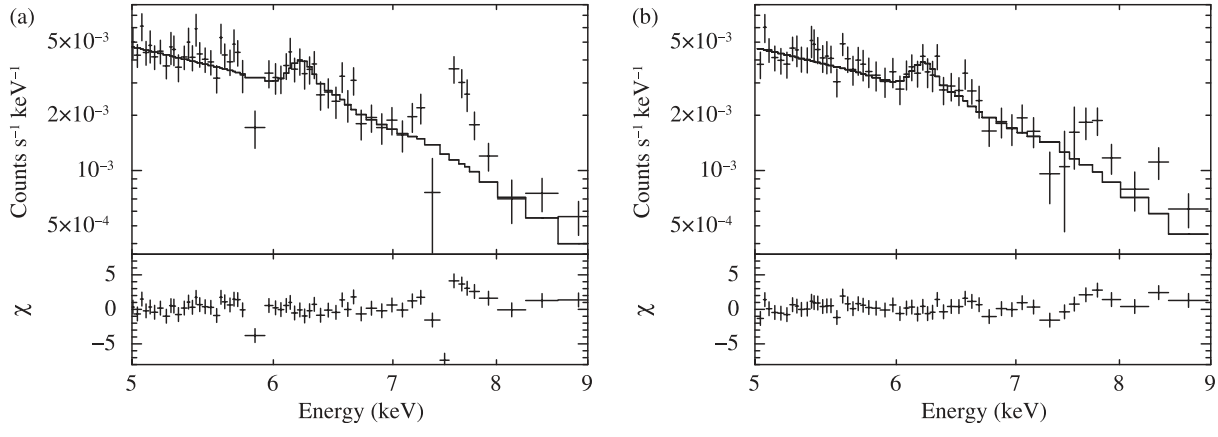

Fig. 11. On-source observation with or without a correction for the emission-line components. (a) Spectrum from which the NXB model spectrum was subtracted without any correction for the emission-line components. (b) Spectrum from which the NXB model spectrum was subtracted with the correction for the emission-line components. These are the averaged spectra of the XIS-FIs.

energy resolution, this simulation needed to be done with the RMF calculated for the epoch of the on-source observation by using the xisrmfgen command in FTOOLS. Xisrmfgen is a response generator for the Suzaku XIS. The normalizations and line center energies of the five Gaussian components were fixed with those obtained in step 2, though radioactive decay of ^{55}Fe was taken into account. The intrinsic widths of these lines were fixed to be zero. We then obtained the NXB model spectrum in which degradation in the energy resolution and the ^{55}Fe decay were taken into account.

The NXB model spectrum with the correction for the emission line components is shown as a green line in figure 10. The line widths of this spectrum are larger than those of the NXB model spectrum without any correction (red line shown in figure 10). Additionally, the intensities of the Mn-K lines decrease with the correction. Figure 11b shows the source spectrum from which the NXB model with the correction for the emission line components was subtracted. The model in figure 11b is the same as that in figure 11a. This correction could reduce the residuals in the energy bands including Mn-Kα and Ni-Kα, and thus improving the reduced χ^2 from 1.77 to 1.16, in this case.

5. Discussion

5.1. Case Study: 100 ks Exposure

In this section, we demonstrate to what extent the uncertainty of the source intensity depends on the NXB reproducibility. We assume an extended source over the XIS FOV, whose surface brightness is comparable to that of the CXB. We also assume an exposure time of 100 ks, typical for this type of extended source. Such an observation typically spans two days, corresponding to an NTE exposure of 5 ks in our database. We concentrate on the of 5–12 keV energy band of XIS-FIs. We find the count rate of the NXB, $I_{\rm NXB}$, to be 5.0×10^{-2} counts s^{-1} and the reproducibility, $\Delta I_{\rm NXB}$, to be 1.8×10^{-3} counts s^{-1} (3.5% of the $I_{\rm NXB}$) based on table 5c. Kushino et al. (2002) measured a CXB power-law photon index of 1.412 and a flux of 6.38×10^{-8} erg cm^{-2} s^{-1} sr^{-1}. They also estimated the spatial fluctuation of the CXB flux to be 6.5% (1σ) by analyzing the ASCA GIS data. Employing these values, we can evaluate the expected count rate for the XIS-FIs, $I_{\rm CXB}$, to be 9.7×10^{-3} counts s^{-1}. We assume that the spatial fluctuation follows the Poisson statistics of the number of sources in the FOV. We can then calculate the spatial fluctuation of the CXB for the XIS FOV to be $6.5\times\sqrt{0.4/0.088}$ = 14%, since the FOVs of the ASCA GIS and the XIS are 0.4 deg^2 and 0.088 deg^2, respectively. Employing an exposure of 100 ks, we can estimate the CXB fluctuation in the XIS, $\Delta I_{\rm CXB}$, to be 1.4×10^{-3} counts s^{-1}. We should note that $\Delta I_{\rm CXB}$ is comparable to $\Delta I_{\rm NXB}$ in our case.

When we obtain the count rate of the raw data, $I_{\rm raw}$, we will subtract NXB and CXB from it in order to evaluate the source count rate, $I_{\rm src}$. Since we assume $I_{\rm src}$ to be comparable to $I_{\rm CXB}$, $I_{\rm raw}$ is $(5.0 + 0.97 + 0.97)\times10^{-2}$ = 6.9×10^{-2} counts s^{-1} and its statistical error, $\Delta I_{\rm raw}$, is 8.3×10^{-4} counts s^{-1}. We will obtain $I_{\rm src}$ by subtracting ($I_{\rm CXB}+I_{\rm NXB}$) from $I_{\rm raw}$. We can calculate the error of $I_{\rm src}$, $\Delta I_{\rm src}$, to be $\sqrt{\Delta I^2_{\rm NXB}+\Delta I^2_{\rm CXB}+\Delta I^2_{\rm raw}} = 2.4\times10^{-3}$ counts s^{-1}. $\Delta I_{\rm NXB}$ and $\Delta I_{\rm CXB}$ contribute almost equally to $\Delta I_{\rm src}$, while the contribution of the statistical error, $\Delta I_{\rm raw}$ is smaller than these two. Similarly, we evaluated the NXB reproducibility of the XIS-FIs in the 1–7 keV energy band by using the same method as employed in the 5–12 keV band. The calculations show that $\Delta I_{\rm NXB} = 1.7\times10^{-3}$, $\Delta I_{\rm CXB} = 8.1\times10^{-3}$, and $\Delta I_{\rm src} = 1.3\times10^{-3}$ (counts s^{-1}). We should note that $I_{\rm NXB}$ does not change very much, while $I_{\rm CXB}$ is 6-times bigger in the 1–7 keV band than that in the 5–12 keV band. Therefore, $\Delta I_{\rm src}$ is mainly determined by $\Delta I_{\rm CXB}$, rather than by $\Delta I_{\rm NXB}$.

5.2. Case Study: Filtering the Data to Reduce the Error of Source Count Rate

We have considered the case of a 100 ks exposure in the subsection mentioned above. Depending on the exposure time and the count rate of the source, the contribution of the statistical error, $\Delta I_{\rm raw}$, to $\Delta I_{\rm src}$ is minor. $\Delta I_{\rm src}$ can be reduced under some conditions by filtering the data as shown below.

We consider a specific example in which the data are filtered with the condition PIN-UD < 225 counts s^{-1}. We call this as a "PIN-UD filter". Using the PIN-UD filter, the exposure time reduces to 85% of that without the filter. The NXB count rate and reproducibility in the 5–12 keV band of the XIS-FIs are 4.6×10^{-2} counts s^{-1} ($I'_{\rm NXB}$) and 3.2% (normalized by $I'_{\rm NXB}$), respectively. These values are based on the *NXB2* data, and this reproducibility is obtained for each 5 ks exposure.

We now derive the condition that the PIN-UD filter provides a smaller $\Delta I_{\rm src}$ than that without the PIN-UD filter for a given on-source observation. We hereafter refer to the error of the source count rate and the NXB reproducibility with the PIN-UD filter as $\Delta I'_{\rm src}$ and $\Delta I'_{\rm NXB}$, respectively. On the other hand, those without the PIN-UD filter are newly defined as $\Delta I_{\rm src}$ and $\Delta I_{\rm NXB}$, respectively. $\Delta I'_{\rm src}$ is expressed as

$$\Delta I'^2_{\rm src} = \Delta I'^2_{\rm NXB} + \Delta I^2_{\rm CXB} + \Delta I'^2_{\rm raw}, \tag{8}$$

$$= (0.032 I'_{\rm NXB})^2 + \Delta I^2_{\rm CXB} + \frac{I_{\rm CXB} + I'_{\rm NXB} + I_{\rm src}}{0.85T}, \tag{9}$$

where $\Delta I'_{\rm raw}$ is the statistical error of the count rate of the raw data with the PIN-UD filter. T is the exposure time of the on-source observation. On the other hand, $\Delta I_{\rm src}$ is expressed as

$$\Delta I^2_{\rm src} = (0.035 I_{\rm NXB})^2 + \Delta I^2_{\rm CXB} + \frac{I_{\rm CXB} + I_{\rm NXB} + I_{\rm src}}{T}. \tag{10}$$

$I_{\rm src}$, $I_{\rm CXB}$, and $\Delta I_{\rm CXB}$ are not altered by the PIN-UD filter. To obtain a value for $\Delta I'_{\rm src}$ that is smaller than that for $\Delta I_{\rm src}$, the condition is expressed as follows:

$$(0.032 I'_{\rm NXB})^2 + \frac{I_{\rm CXB} + I'_{\rm NXB} + I_{\rm src}}{0.85T} < (0.035\, I_{\rm NXB})^2 + \frac{I_{\rm CXB} + I_{\rm NXB} + I_{\rm src}}{T}, \tag{11}$$

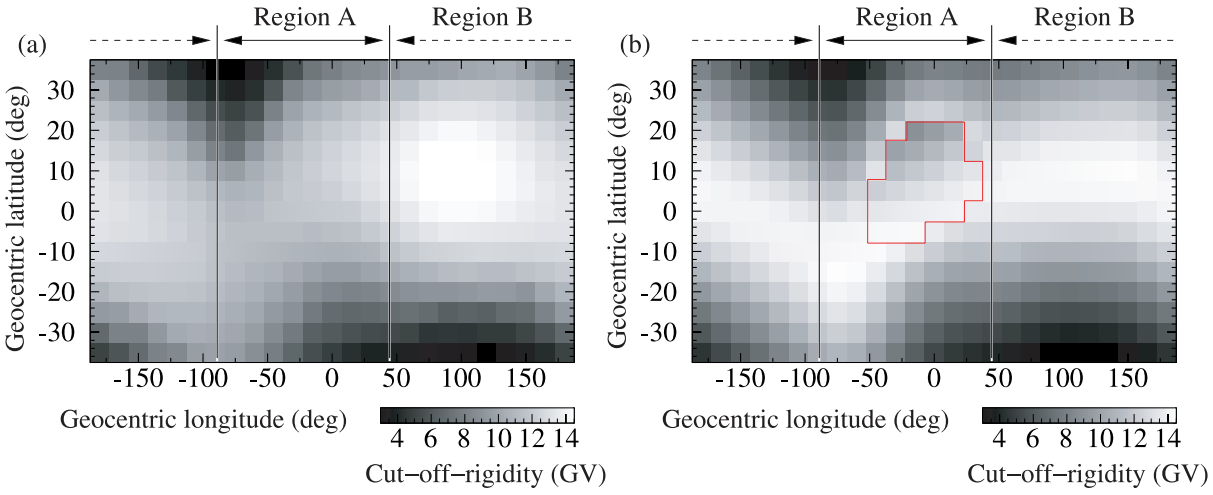

Fig. 12. Maps of (a) the *COR* and (b) the *COR2*. The region A is $-90° <$ latitude $< 45°$, and the region B encompasses the remaining latitude range.

$$I_{\rm src} < 5.1 \times 10^{-3} \left(\frac{T}{1\,{\rm ks}} \right) - 0.033 \ {\rm cts\ s^{-1}} \ . \qquad (12)$$

The term $\Delta I^2_{\rm CXB}$ vanishes from both sides of the above inequality.

In the case that the exposure time of the on-source observation is 100 ks, the PIN-UD filter is effective for a diffuse source whose count rate is less than 0.48 counts s^{-1}. This count rate corresponds to 49-times that of the CXB. On the other hand, if the exposure time is 20 ks, the PIN-UD filter is effective only for a source whose count rate is lower than 7.1-times that of the CXB.

6. Summary

We constructed the NXB database by collecting the XIS events of the NTE. The NXB database, accompanied with EHK files, and two software tools, mk_corsorted_spec_v1.0.pl and mk_corweighted_bgd_v1.1.pl, are now accessible via the Suzaku web page at ISAS/JAXA and GSFC/NASA. Since the XIS NXB depends on the cut-off-rigidity in orbit or on the PIN-UD count rate, we need to equalize the distributions of these parameters for the on-source observations and for the NTE observation, so that we can actually subtract the NXB. We have examined two modeling parameters to model the NXB, *COR2* and PIN-UD. We find a large deviation of the NXB count rate from that expected from both models when Suzaku passes through high-altitude and high-latitude regions. Excluding those data, the NXB reproducibilities are significantly improved. Similarly, excluding the data taken in 2005 September, the reproducibility for the XIS 2 is improved. Our results show that the NXB model sorted by the PIN-UD has a better reproducibility than that by *COR2*. Using the NXB data in 5 ks exposure bins, the reproducibility obtained with the PIN-UD model is 4.55–5.63% for each XIS NXB in the 1–7 keV band and 2.79–4.36% for each XIS NXB in the 5–12 keV band. This NXB reproducibility in 5–12 keV, 1.8×10^{-3} counts s^{-1}, is comparable to the spatial fluctuation of the CXB for the XIS FOV, 1.4×10^{-3} counts s^{-1}. The NXB reproducibility and the spatial fluctuation of the CXB were evaluated to be 1.7×10^{-3} counts s^{-1} and 8.1×10^{-3} counts s^{-1}, respectively, in the 1–7 keV band. Depending on the exposure time and the count rate of the source, the statistical error of the raw data is much smaller than the NXB reproducibility. In such a case, the error of the source count rate can be reduced by excluding data with a high NXB count rate (e.g., filtering with PIN-UD < 225 counts s^{-1}).

Note added in proof (2008 January 10):
The tools to generate the NXB model, mk_corsorted_spec_v1.0.pl and mk_corweighted_bgd_v1.1.pl, introduced in the subsection 2.1 are now obsolete. Their function was succeeded by a single tool, xisnxbgen. The tool has a standard FTOOLS interface as for other Suzaku FTOOLS, and has more flexibility in parameter selection than the previous two tools. The first version of xisnxbgen was released as one of Suzaku FTOOLS version 7 as a part of HEAsoft 6.4 on 2007 December 7. Correspondingly, the NXB database is now included in the Suzaku CALDB and will be updated for every several months so as to include latest NXB data. See the web site given in a footnote.[5]

The authors wish to thank all of the XIS team members for their support, help, and useful information. This work is partly supported by Grants-in-Aid for Scientific Research by the Ministry of Education, Culture, Sports, Science and Technology of Japan (16002004 and 1910350). This study is also carried out as part of the 21st Century COE Program, '*Towards a new basic science: depth and synthesis*'. N. T. is supported by JSPS Research Fellowship for Young Scientists.

Appendix 1. New and Old Maps for the Cut-off-Rigidity

The cut-off-rigidity values were calculated from the orbital position of Suzaku using a cut-off-rigidity map, shown in figure 12a. However, the map assumes charged particles originating from the zenith direction at an altitude of 500 km, and it uses an international geomagnetic reference field for 1975.

[5] ⟨http://heasarc.nasa.gov/docs/suzaku/analysis/suzaku_ftools.html⟩.

Table 8. Reproducibility of the NXB model with the *COR*.*

Sensor	Reproducibility of *COR* (%)			
	5 ks exposure		50 ks exposure	
	1–7 keV†	5–12 keV‡	1–7 keV†	5–12 keV‡
XIS 0	5.73 ± 0.76	4.46 ± 0.64	2.28 ± 0.88	1.60 ± 0.72
XIS 1	7.97 ± 0.73	6.60 ± 0.51	3.42 ± 0.94	3.12 ± 0.75
XIS 2	7.63 ± 0.85	5.60 ± 0.68	1.70 ± 0.84	2.02 ± 0.77
XIS 3	6.58 ± 0.85	3.20 ± 0.65	2.14 ± 0.92	1.15 ± 0.72

* In the energy bands of 1–7 keV and 5–12 keV.
† These values are normalized by the average count rates shown in table 6.
‡ These values are normalized by the average count rates shown in table 4.

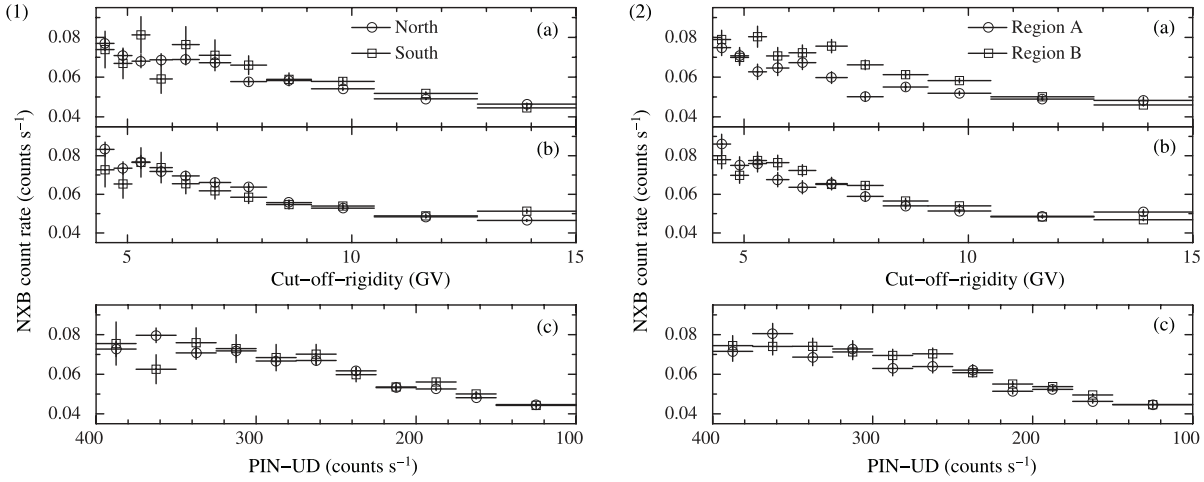

Fig. 13. NXB of the XIS 0 for given values of (a) *COR*, (b) *COR2*, and (c) PIN-UD. (1) shows the NXB count rates for the northern and southern hemisphere separately. The open circles are for the north hemisphere and open squares for the south hemisphere. (2) shows the count rates for region A and the region B (see figure 12). The open circles are for region A and the open squares for region B.

This cut-off-rigidity definition (hereafter "*COR*") is out of date and inaccurate. We therefore define a new cut-off-rigidity map based on the recent cut-off-rigidity database.

The new cut-off-rigidity map is calculated by using corrected geomagnetic (CGM) coordinates. The CGM coordinates are useful to study geophysical phenomena affected by the Earth's magnetic field, and are provided at the web service by NASA[6] (Tsyganenko 1996). To calculate the CGM coordinates, several parameters are required. We set these parameters as follows: the altitude is 570 km, the date is 2006/01/01 00:00:00, and the default parameters are employed for the solar wind (Den = 3, Vel = 400, BY = 5, BZ = −6, and Dst = −30). Then, the new cut-off-rigidity value, $R_{\rm C}$, is calculated as follows,

$$R_{\rm C} = 14.5 \frac{\cos^2 \theta}{r^2} \quad {\rm GV}, \tag{A1}$$

where θ is the latitude in CGM coordinates. r is the distance from the center of Earth's magnetism, and the value of r is normalized by the radius of Earth. We call this cut-off-rigidity "*COR2*". Figure 12b shows a *COR2* map. In the red box region shown in figure 12b, since the CGM cannot be obtained due to the local magnetic structure, we use the geomagnetic latitude obtained with a dipole approximation in place of the CGM.

The cut-off-rigidity value for each event can be determined from the EHK file associated with each observation. The EHK files before revision 2.0 processing contain only *COR*, while those after revision 2.0 contain both *COR* and *COR2*. These *COR* and *COR2* values are calculated using the cut-off-rigidity maps of rigidity_20000101.fits and rigidity_20060421.fits in the generic area of the calibration database (CALDB).

We evaluate the reproducibility of the NXB model with *COR* in the same way as that with *COR2* or PIN-UD as described in the main text. The bin ranges of the *COR* to sort the NXB data and on-source data are the same as the *COR2* as shown in table 3. Table 8 gives the reproducibility of the NXB model with *COR* in the energy bands of 1–7 keV and 5–12 keV. The reproducibility was calculated by dividing the *NXB2* data into 5 ks or 50 ks exposure bins. We found that *COR* has the worst reproducibility among the three kinds of NXB models.

We searched for the location where the *COR* does not perfectly reproduce XIS NXB. Figure 13(1) shows the average count rate of XIS 0 NXB in the 5–12 keV energy band as

[6] The service is available at ⟨http://modelweb.gsfc.nasa.gov/models/cgm/t96.html⟩.

a function of the three modeling parameters, in the northern hemisphere and in the southern hemisphere, displayed separately. This count rate is obtained from the *NXB2* data. For the three modeling parameters, there is not a large difference between the NXB count rate in the northern hemisphere and that in the southern hemisphere. On the other hand, if we take the data from two different longitude regions, region A and region B in figure 12, we obtain figure 13 (2). There is a significant difference between the NXB count rate in region A and that in region B for a given value of *COR*. This is one reason *COR* gives the worst reproducibility.

Appendix 2. Errors of the Statistical Parameters

We discuss the errors of $\sigma_{\rm c}$, $\sigma_{\rm sta,c}$, $\sigma_{\rm sys,c}$, and $\sigma_{\rm sys,\Delta c}$, as defined in subsection 3.2. If the distribution of C_j follows a Gaussian distribution, whose average and standard deviation are μ and σ, respectively, then $(n-1)\sigma_{\rm c}^2/\sigma^2 \equiv X$ follows a χ^2 distribution with $(n-1)$ degrees of freedom. The expected value and variance of X are $(n-1)$ and $2(n-1)$, respectively. Although the distribution of the statistical error of X does not correctly follow a Gaussian distribution, the statistical error can be approximated with $\sqrt{2(n-1)}$. Thus, the statistical error of $\sigma_{\rm c}^2$ is $\sigma^2\sqrt{2/(n-1)}$. However, since σ is a standard deviation of the parent population, and can not be obtained, we approximate that σ equals $\sigma_{\rm c}$. As a result, the statistical error of $\sigma_{\rm c}^2$ is $\sigma_{\rm c}^2\sqrt{2/(n-1)}$. The statistical error of $\sigma_{\rm c}$ ($\Delta\sigma_{\rm c}$) is expressed by using the principle of error propagation as follows:

$$\Delta\sigma_{\rm c} = \frac{\sigma_{\rm c}}{\sqrt{2(n-1)}}\,. \tag{A2}$$

In the same way, the statistical error of $\sigma_{\rm sta,c}$ ($\Delta\sigma_{\rm sta,c}$) is obtained as follows:

$$\Delta\sigma_{\rm sta,c} = \frac{\sigma_{\rm sta,c}}{\sqrt{2(n-1)}}\,. \tag{A3}$$

The statistical errors of $\sigma_{\rm sys,c}$ ($\Delta\sigma_{\rm sys,c}$) is expressed by using the principle of error propagation as follows:

$$\Delta\sigma_{\rm sys,c} = \frac{1}{\sigma_{\rm sys,c}\sqrt{2(n-1)}}\sqrt{\sigma_{\rm c}^4+\sigma_{\rm sta,c}^4}\,. \tag{A4}$$

In the same way as $\Delta\sigma_{\rm sys,c}$, the statistical error of $\sigma_{\rm sys,\Delta c}$ ($\Delta\sigma_{\rm sys,\Delta c}$) is expressed as follows:

$$\Delta\sigma_{\rm sys,\Delta c} = \frac{1}{\sigma_{\rm sys,\Delta c}\sqrt{2(n-1)}}\sqrt{\sigma_{\rm \Delta c}^4+\sigma_{\rm sta,\Delta c}^4}\,. \tag{A5}$$

References

Burke, B. E., Mountain, R. W., Harrison, D. C., Bautz, M. W., Doty, J. P., Ricker, G. R., & Daniels, P. J. 1991, IEEE Trans. ED, 38, 1069

Carter, J. A., & Read, A. M. 2007, A&A, 464, 1155

Fujimoto, R., et al. 2007, PASJ, 59, S133

Fujita, Y., Tawa, N., Hayashida, K., Takizawa, M., Matsumoto, H., Okabe, N., & Reiprich, T. H., 2008, PASJ, 60, S343

Hasinger, G., et al. 2001, A&A, 365, L45

Ishisaki, Y., et al. 2007, PASJ, 59, S113

Kokubun, M., et al. 2007, PASJ, 59, S53

Koyama, K., et al. 2007, PASJ, 59, S23

Kushino, A., Ishisaki, Y., Morita, U., Yamasaki, N. Y., Ishida, M., Ohashi, T., & Ueda, Y. 2002, PASJ, 54, 327

Lumb, D. H., et al. 2000, Proc. SPIE, 4140, 22

Mitsuda, K., et al. 2007, PASJ, 59, S1

Mizuno, T., Kamae, T., Godfrey, G., Handa, T., Thompson, D. J., Lauben, D., Fukazawa, Y., & Ozaki, M. 2004, ApJ, 614, 1113

Snowden, S. L., et al. 1997, ApJ, 485, 125

Takahashi, T., et al. 2007, PASJ, 59, S35

Tsyganenko, N. A. 1996, in Proc. Third Int. Conf. on Substorms (ICS-3) ESA SP-389, 181

Weisskopf, M. C., Brinkman, B., Canizares, C., Garmire, G., Murray, S., & Van Speybroeck, L. P. 2002, PASP, 114, 1

Yamaguchi, H., et al. 2006, Proc. SPIE, 6266, 626642